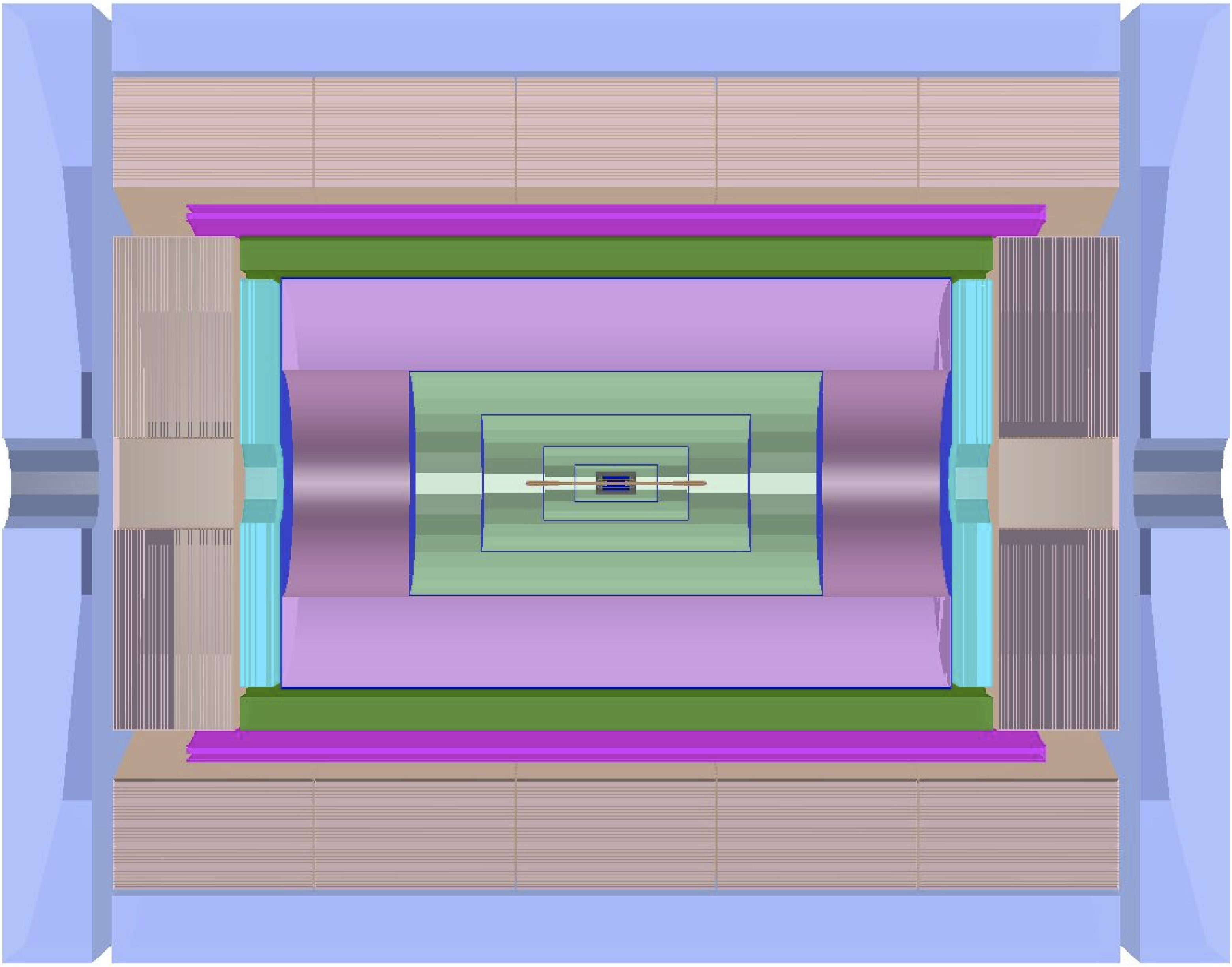

TDR:performance

Technical Design Report of the CEPC Reference Detector

Author: the CEPC study group
Institute:
Date: June 9, 2025
Version: 0.1
Bio: Information

Contents

Chapter 1 Detector and Physics performance

1.1 Introduction

The overall performance of the CEPC Reference TDR detector is established using a detailed GEANT4 model [ref] and full reconstruction of the simulated events. Using full simulation and a realistic reconstruction ensures that the performance is as realistic as possible and takes into account the detailed knowledge on detector mechanics, dead areas, and non-perfect response.

In this chapter the physics objects performance of the CEPC detector is discussed. Then a series of different physics studies done using full Monte Carlo at different center of mass energies from 91 to 350 GeV are presented. These analyses have not been selected to demonstrate the physics reach at CEPC, but rather to stress the detector and its performance.

Most of the sub-detectors have been implemented with a significant amount of engineering detail such as mechanical support structures, electronics and cabling as well as dead material and cracks. The material budget associated with the support structures and services are based on the best current estimates from the detector R&D groups. In addition, the material associated with the delivery of power and cooling to the sub-detectors have been implemented in the simulation so as to provide a reasonable description of the mean material budget. A description of the detector parameters and the reconstruction software can be found in the Software Chapter.

All events are reconstructed based on a sophisticated reconstruction chain, including using a Kalman-filter based track reconstruction and the CyberPFA particle flow algorithm.

1.2 Detector Performance

To evaluate the performance of the CEPC detector concept and the reconstruction software as relevant for the benchmarking analyses, tracking, PID, vertex reconstruction and flavor tagging, and performance of the particle flow algorithms have been studied in detail.

1.2.1 Tracking (Chenguang Zhang, Hao Zhu, et al.)

CEPC ref-TDR tracking is designed around three subsystems capable of standalone tracking: VTX, Silicon Tracker (ITK) and the TPC. These are augmented by one auxiliary tracking system, the OTK, which provide additional high resolution measurement points. The TPC provides full coverage down to $\theta \approx 37^\circ$. Beyond this the number of measurement points decreases. The last measurement point provided by the TPC corresponds to $\theta \approx 10^\circ$. The central inner tracking system, consisting of the six layer VTX and the three layer ITK , provides 9 precise measurements down to $\theta \approx 37^\circ$. The ITK endcap provides up to a maximum of 4 measurement points for tracks at small polar angles. The OTK provide a single high precision measurement point with large lever arm outside of the TPC volume down to a $\theta \approx 8.5^\circ$.

1.2.1.1 Tracking efficiency

With over 200 continuous readout layers, pattern recognition and track reconstruction in a TPC is relatively straightforward, even in an environment with a large number of background hits. In addition, the standalone tracking capability of the VTX+ITK enables the reconstruction of low transverse momentum tracks which do not reach the TPC. ITK endcap coverage enables tracks to be reconstructed to polar angles below $\theta \approx 8.5^\circ$.

Figure 1.1 shows, as a function of momentum and polar angle, the track reconstruction efficiency in simulated (high multiplicity) ZH → 4 jets at $\sqrt{s}$ = 240 GeV. Efficiencies are plotted with respect to MC tracks that stem from a region of 10 cm around the IP with pt $>$ 100 MeV and $\cos(\theta) > 0.99$, excluding decays in flight and requiring at least 90% purity. For the combined tracking system, the track reconstruction efficiency is on average 99.7% for tracks with momenta greater than 1 GeV across the entire polar angle range, and it is larger than 99.8% for $\cos(\theta) < 0.95$.

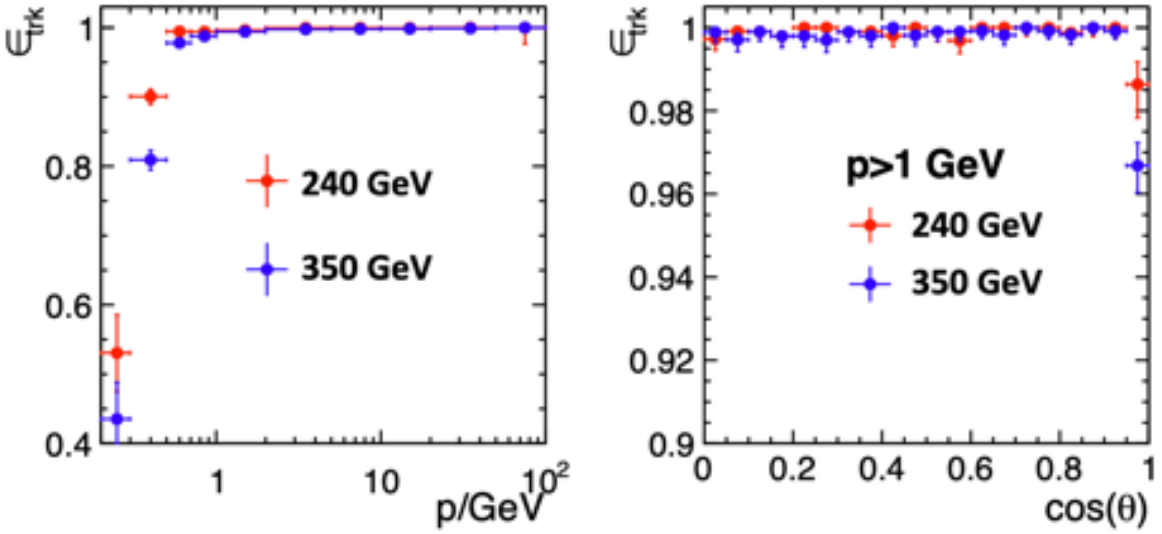

Figure 1.1: Track efficiency for ZH → 4 jets at 240 GeV plotted against (left) momentum and (right) cos(θ).

Fig. 1.2 shows the track efficiency in the low momentum region for ZH → 4 jets at 240 GeV, as a function of either momentum (left) or transverse momentum (right) and cos(θ).

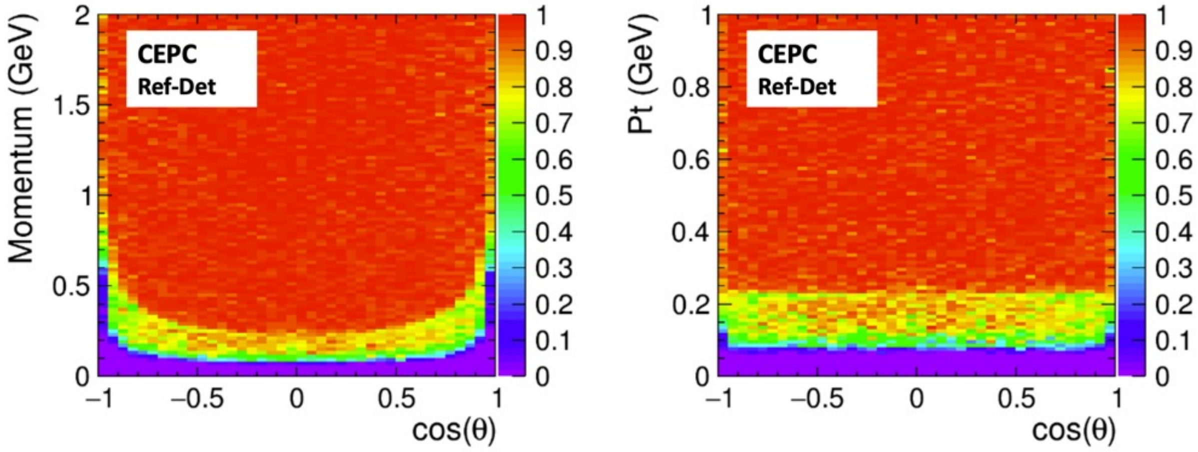

Figure 1.2: Track efficiency in the low momentum region for ZH → 4 jets at 240 GeV plotted against 2D plane of momentum (left) or transverse momentum (right) vs. cos(θ).

The effects of background from beam background events are taken into account by overlaying the corresponding number of events.

1.2.1.2 Momentum resolution

Figure 1.3 left shows track momentum resolutions for different configurations: Vertex+ITK+OTK, TPC, Vertex+ITK+TPC, Vertex+ITK+TPC+OTK.

The momentum resolution with the CEPC ref-detector simulation and full reconstruction is shown in Figure 1.3 right. The study was performed using muons generated at fixed polar angles of $\theta = 10°, 20°, 40°$ and $85°$, and the momentum was varied over the range $1 \sim 100$ GeV. For one polar angle, this is compared to the expected parametric form of $\sigma_{1/p_T} = a \oplus b/(p_T sin\theta)$, with $a = 2 \times 10^{-5}$ GeV^{-1} and $b = 1 \times 10^{-3}$. As can be seen, at a polar angle of 85°, the required momentum resolution is attainable over the full momentum range from 1 GeV upwards. This remains true over the full length of the barrel region of the detector, where the TPC in conjunction with the OTK is able to provide the longest possible radial lever arm for the track fit. For high momentum tracks, the asymptotic value of the momentum

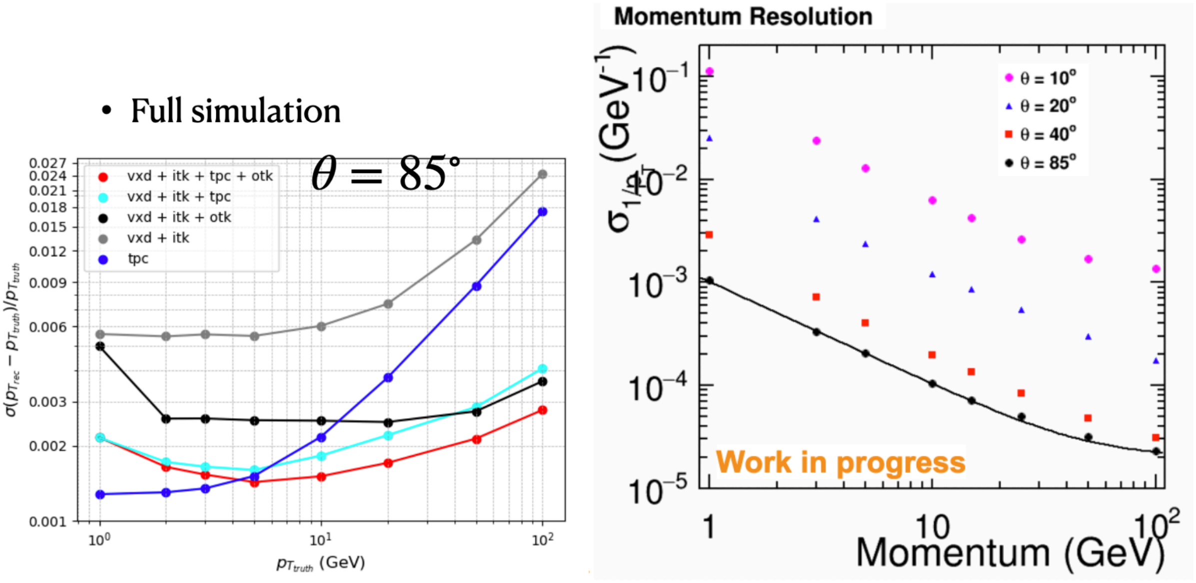

Figure 1.3: (Left) Track resolution for different detector configurations. (Right) Transverse momentum resolution for single muon events as a function of the transverse momentum for different polar angles. The lines show $\sigma_{1/p_T} = 2 \times 10^{-5} \oplus 1 \times 10^{-3}/(p_T sin\theta)$.

resolution is $\sigma_{1/p_T} = 2 \times 10^{-5}$ GeV^{-1}. In the very forward region, the momentum resolution is inevitably worse due to the relatively small angle between the B-field and the track momentum.

1.2.1.3 Impact parameter resolution

Figure 1.4 left shows rphi impact parameter resolution as a function of the transverse track momentum. The required performance is achieved down to a track momentum of 1 GeV, whilst it is exceeded for high momentum tracks where the asymptotic resolution is 2 µm. Figure 1.4 right shows rz impact parameter resolution, which is better than $\geq$ 10 µm down to momenta of 3 GeV and reaches an asymptotic value of $\leq$ 5 µm for the whole barrel region. The impact parameter resolution here assumes perfect alignment of the tracking systems.

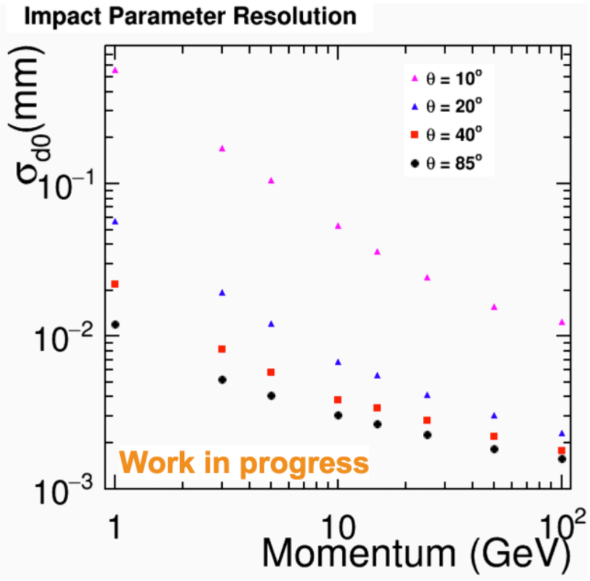

PLACEHOLDER
plot

Figure 1.4: Impact parameter resolution for single muon events as a function of the transverse momentum for different polar angles, d0 in left and dz in right.

1.2.2 PID

1.2.2.1 Photon, Electron and Muon **(Ligang Xia, Danning Liu, et al.)**

Particle identification (particle ID), and in particular lepton identification will be central to many physics studies at the CEPC. Methods for phone and leptons identification using calorimeter shower shapes have been developed. Muons are identified and all of their hits removed before the calorimeter hits are clustered. The track-cluster agreement is optimised using various re-clustering strategies, which are guided by identifying the cluster as belonging to an electromagnetic or a hadronic interaction.

The particle identification has been evaluated on samples of single photons, electrons, muons and pions of 1, 2, 5, 10, 20, 30, 45, 60, 80 GeV, respectively (see Figures 1.5-1.7 below). In these plots, the reconstructed particle is required to have the same type as the generated particle, and for electrons and pions a loose energy cut of five times the resolution of the EM calorimeter above or below the energy of the generated particle is applied. .

The default for neutral particles is the neutron hypothesis, while charged particles are assigned the pion hypothesis by default. The muon identification efficiency is above XX% for values of the polar angle $10° \leq \theta \leq 170°$. The photon identification efficiency is above XX% over the same angular range, except for an inefficiency in the transition region between calorimeter barrel and endcap, which results in a dip in the bin $30° \leq \theta \leq 40°$. That same region results also in a dip of the electron efficiency, which is otherwise over XX% for XX GeV electrons.

The performance of the reconstruction as shown here has not been optimised for particle identification efficiency, but rather for jet energy resolution. We expect that a significant improvement can be achieved - particularly in the transition region between calorimeter barrel and endcap - with dedicated particle identification algorithms that are optimised for performance with the TPC/TOF and Glass Scintilator HCal.

PLACEHOLDER
plot

Figure 1.5: Identification efficiency for photons as a function of the angle theta for different energy points: 1, 2, 5, 10, 20, 30, 45, 60, 80 GeV separately.

1.2.2.2 Charged Hadrons **(Chenguang Zhang, Xiaotian Ma, et al.)**

Measuring the energy loss of charged particles in the TPC provides a powerful tool for identifying the type of the particle. In addition, the time of flight measurement from the TOF enhances the identification, in particular for low momentum region around 1 GeV.

Figure 1.6: Identification efficiency for electrons as a function of the angle theta for different energy points: 1, 2, 5, 10, 20, 30, 45, 60, 80 GeV separately.

Figure 1.7: Identification efficiency for muons as a function of the angle theta for different energy points: 1, 2, 5, 10, 20, 30, 45, 60, 80 GeV separately.

Figure 1.8 shows the dE/dx reconstructed from a truncated mean for charged particle tracks in the TPC as a function of the particle momentum, clearly revealing the bands of the most abundant particle types $e^{\pm}, \mu^{\pm}, \pi^{\pm}, k^{\pm}$ and $p^{\pm}$. By fitting Gaussian distributions, with mean $\mu(p)$ and standard deviation $\sigma(p)$, to individual bands in momentum bins one can define a separation power $S_{A,B}$ for distinguishing the two particle types A and B:

$$S_{A,B}(p) = \frac{|\mu_A(p) - \mu_B(p)|}{\sqrt{\frac{1}{2}\left(\sigma_A^2(p) + \sigma_B^2(p)\right)}} \tag{1.1}$$

Figure 1.9 shows the separation power for π, k and K, p based on the dE/dx measurement in the TPC and the improvement achieved by combining it with the time-of-flight (TOF) measurement.

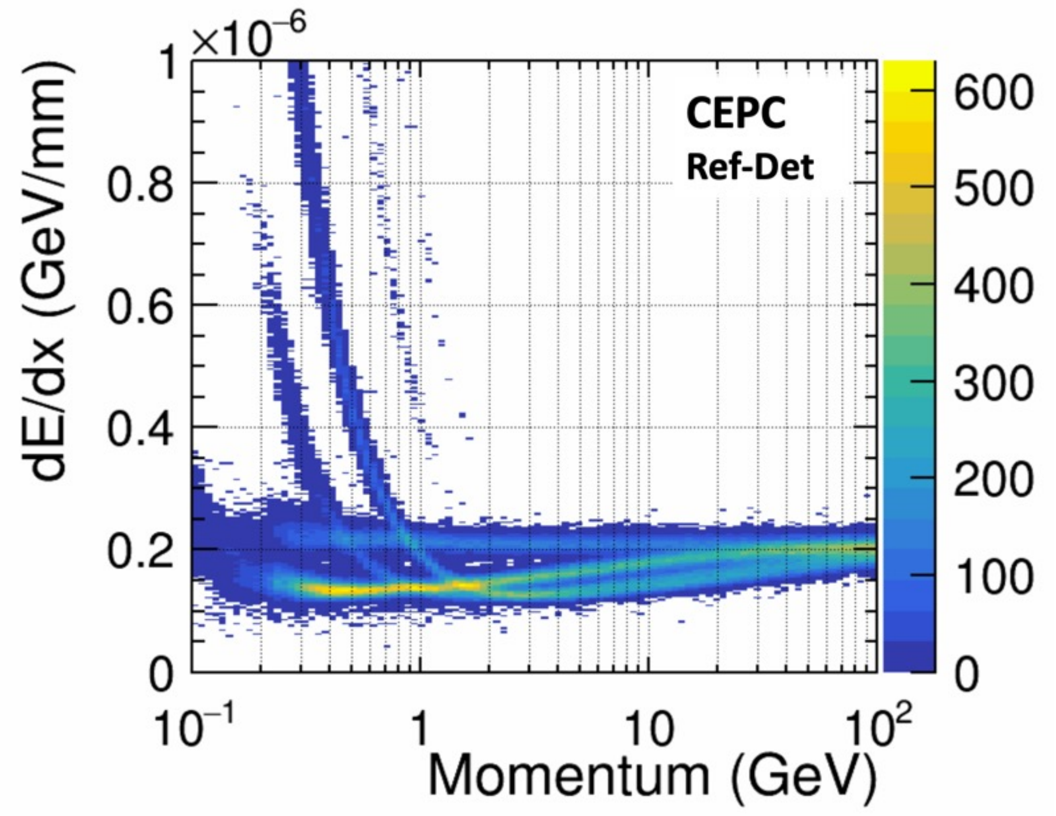

Figure 1.8: dE/dx as a function of particle momentum as reconstructed from a full simulation of single particle events (e, μ, π, K and p) in the TPC.

Figure 1.10 shows the performance of the charged Kaon identification based on dE/dx for TPC and on the combined information from TPC+TOF, as obtained from the Z(qq) events.

1.2.3 Jets (Kaili Zhang, Xiaotian Ma, Yingqi Hou, Chenguang Zhang, Jiarong Li, et al.)

The design of the CEPC detector concept has been optimised for jet energy resolution using the particle flow approach, which requires strong interplay among various sub-detectors and has led to the choice of calorimeters with a high degree of segmentation and transverse granularity. In addition, sophisticated reconstruction algorithms are necessary to obtain a jet energy resolution that allows to separate W and Z decays. The performance is evaluated with Z and ZH samples.

The ee-kt algorithm (a.k.a. Durham algorithm [**??**]) is used as the baseline jet clustering algorithm at the CEPC using the FastJet package [**??**]. "GenJets" are the clustered true-level Monte Carlo particles that were produced from the hadronization of the partons, simulated by Pythia [**??**], including the subsequent decay products such as photons, leptons, or other lighter hadrons. Neutrinos are excluded in the clustering, while only the decay products of hadrons with $c\tau \geq 1$ cm are included. "RecoJets" are clustered from the reconstructed final-state particles by the ee-kt algorithm in the same way as the "GenJet".

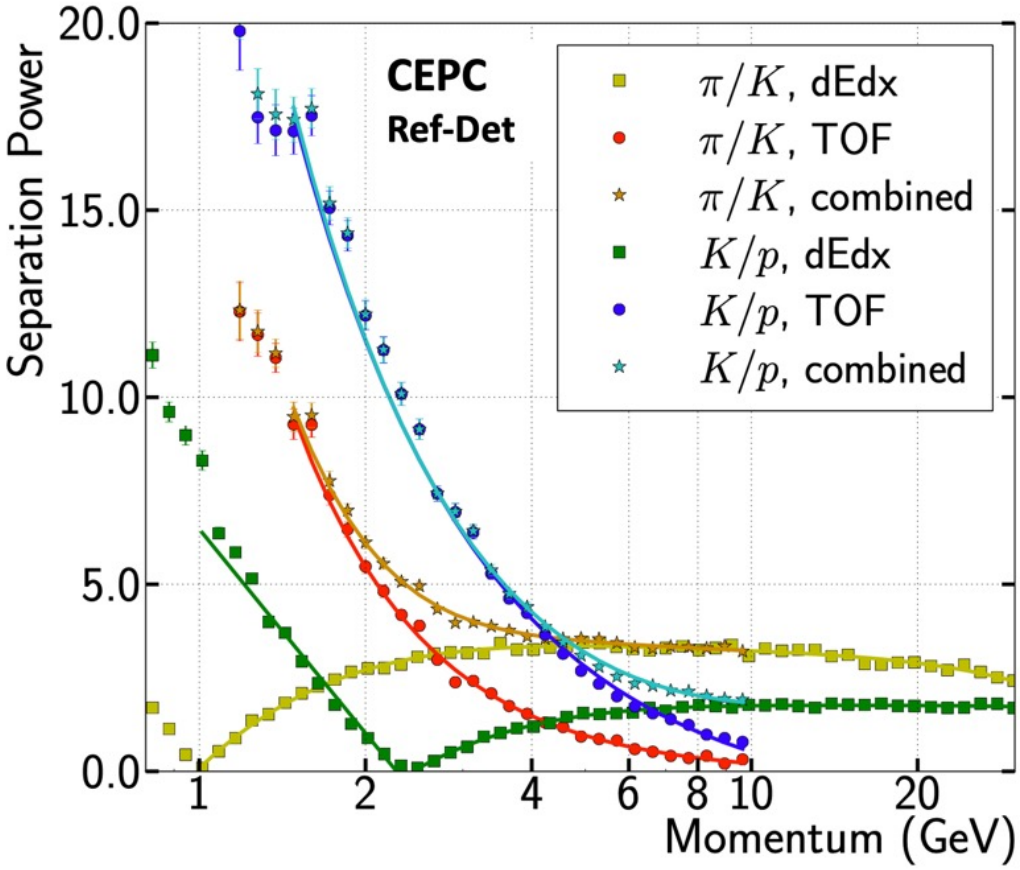

Figure 1.9: Particle separation power (eq. 1.1) for π/K and K/p based on the dE/dx measurement in the TPC (in square) and through TOF (in circle), as well as the combined separation power (in star) where $S_{dE/dx,TOF} = S_{dE/dx} \oplus S_{TOF}$. The curves are shown to guide the eye.

1.2.3.1 Actual Jet Energy Resolution

First the jet energy resolution (JER) without the effects from jet finding or background is studied as shown in Fig. 1.11, to distinguish the measurement of the actual JER from other effects like ISR-photons or confusion in jet clustering that occur in more complex, realistic events. This is done with dedicated $Z \to qq$ events, $q \in [u, d, s]$, where the Z is chosen to have the desired mass of twice the jet energy and decays at rest.

To avoid a bias from possible tails, the rms90 value is computed to describe the energy resolution. It is defined as the standard deviation of the distribution in the smallest range that contains 90% of the events. The jet energy resolution (rms90) is better than X.X% for jets of energy greater than 40 GeV. The resolutions quoted in terms of rms90 should be multiplied by a factor of approximately 1.1 to obtain an equivalent Gaussian analysing power.

Due to the calorimetric coverage in the forward region, the jet energy resolution remains good down to $\theta = XX^\circ$ $(cos\theta = 0.9XX)$ as shown in Fig. 1.11 right.

1.2.3.2 Jet performance in physics events

Then the jet reconstruction performance of several major standard model hadronic processes at the CEPC, including $Z \to qq$ at Z-pole, $ZH \to \nu\nu(qq$ or $gg)$ or $q\bar{q}(q\bar{q}$ or $gg)$ at $\sqrt{s} = 240$ GeV is analyzed.

The GenJet and RecoJet are mapped to each other with the combination that minimizes the sum of angles between the GenJet-RecoJet pairs. For a given pair, the relative difference is then expressed in terms of the jet energy resolution, the jet energy scale (JES), the jet angular resolution (JAR), and the jet angular scale (JAS). The relative energy difference is modelled with the double-sided crystal ball (DBCB) function. The angular (polar and azimuth angle) differences of the GenJet-RecoJet pairs are modelled with the Gaussian function. The JER/S are extracted from the standard deviation

PLACEHOLDER
plot

Figure 1.10: Efficiency-purity curves for charged Kaon identification in the context of the single Z(qq) sample. For the same efficiency, TPC+TOF reaches a XX% higher purity in comparison with TPC only.

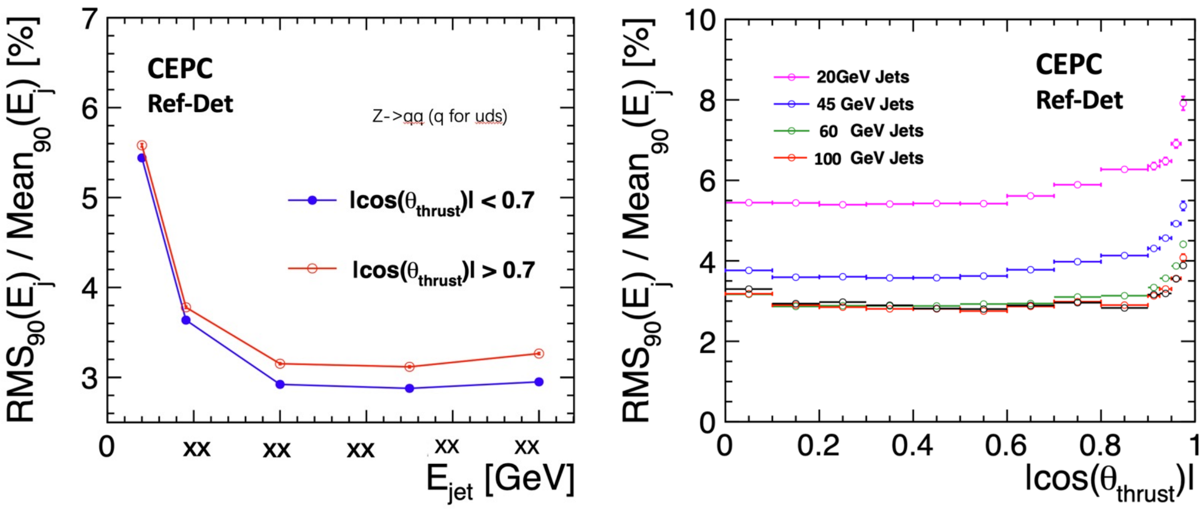

Figure 1.11: Fractional jet energy resolution plotted against jet energy (left) and $|cos\theta|$ (right) where θ_{thrust} is the thrust axis of the event.

(σ) and mean ($\bar{x}$) of the DBCB fitting to the relative energy difference between RecoJet and GenJet while JAR/S are the $\sigma/\bar{x}$ of the Gaussian fitting within $\bar{x} \pm 1.5\sigma$ of angular difference. Fig. 1.12 shows the differential jet energy resolution as functions of the cosθ_{Gen}, azimuth angle and GenJet energy of the above-mentioned physics benchmark processes. The JER is around 4–5% in the barrel region, while JES is controlled within $\pm1\%$ after the jet energy is calibrated by the ratio of the Z-boson mass affected by double counting to the anticipated Z-boson mass from the ZZ semi-leptonic process. This is the first order method to calibrate the PFA double-counting effect.

Fig. 1.13 left shows a comparison of the distributions of the reconstructed Z mass in Z-pole events simulated with and without background. The effect of the background on the reconstructed mass is partially mitigated by the jet clustering. The addition of background from $\gamma\gamma \rightarrow$ hadrons events and incoherent pairs results in only a minor change in resolution in these events. The difference can be explained by the additional background energy in the reconstructed jets balancing the small reconstruction bias towards lower energies in events without background.

Fig. 1.13 right shows a neat separation between the W, the Z, and the Higgs bosons with hadronic final states in their reconstructed invariant mass spectrum.

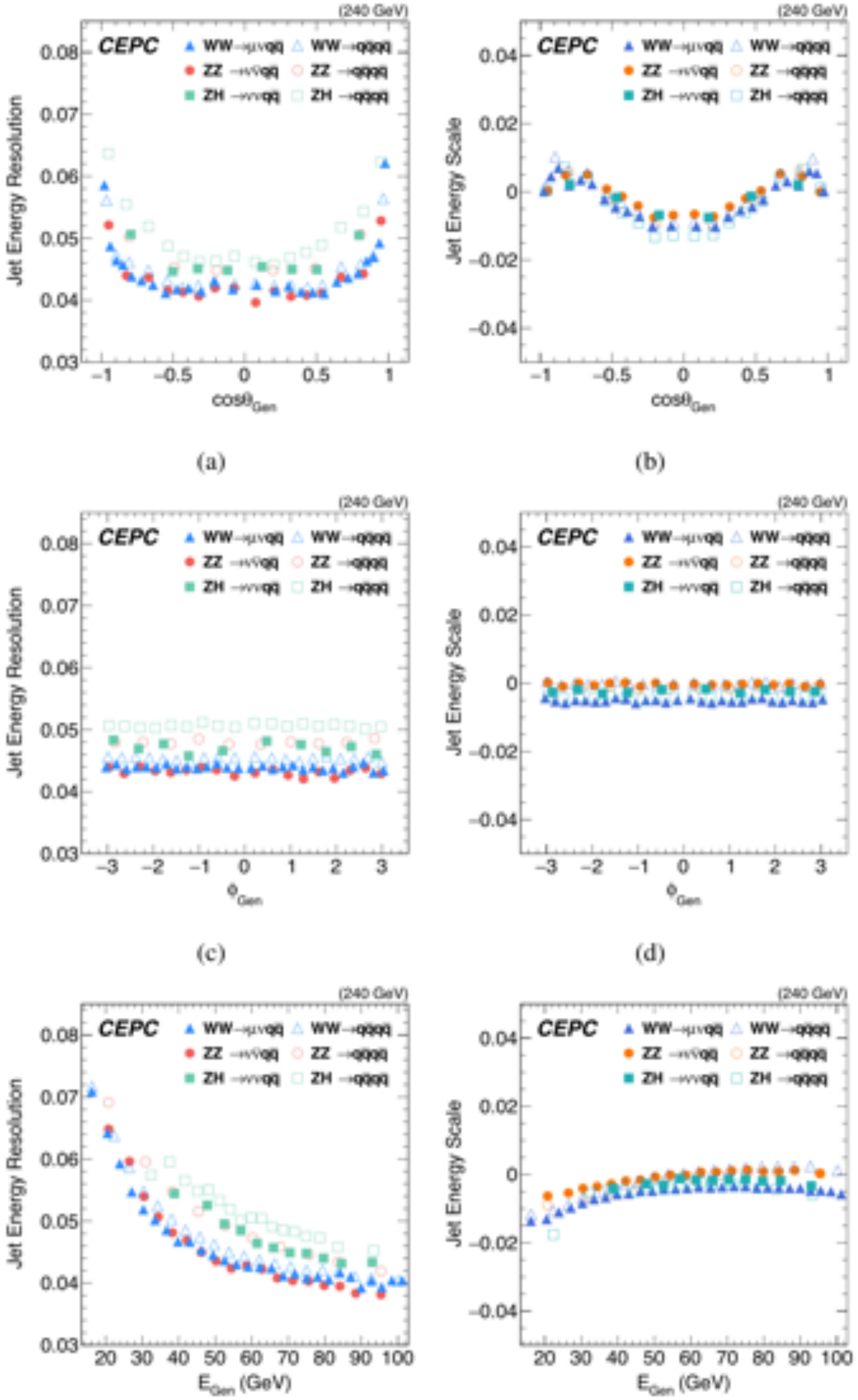

(a) (b)

(c) (d)

(e) (f)

Figure 1.12: Jet energy resolution and scale as functions of (a) and (b) the $\cos\theta_{Gen}$, (c) and (d) the azimuth angle, and (e) and (f) the GenJet energy for 2- (solid symbols) and 4-jet (open symbols) final states. The errors shown are only statistical. In (a) and (b), the jet energy resolutions grow and jet energy scales decrease because part of jet is out of the fiducial acceptance of the detector.

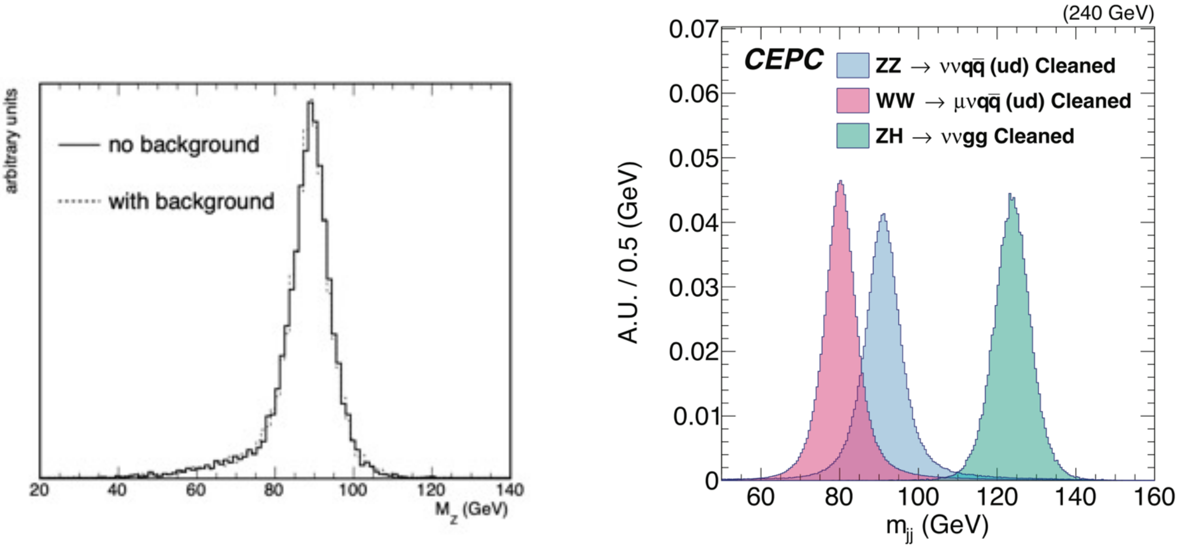

Figure 1.13: (left) Comparison of the distributions of the reconstructed Z mass in Z-pole with and without background. (right) Reconstructed di-jet mass distribution from WW, ZZ and ZH processes at $\sqrt{s} = 240$ GeV.

1.2.4 Vertexing (Chenguang Zhang, et al.)

One of the most important variables in jet flavour tagging networks is the decay length of the secondary vertices, which requires a precise measurement of the coordinates of secondary vertices.

1.2.4.1 Vertex Efficiency

1.2.4.2 Vertex Resolution

The vertex resolution of the CEPC vertex detector has been assessed in the context of the analysis of the ZH samples. Figure 1.14(left) shows the position of the reconstructed primary vertex in events containing two isolated leptons and two b quarks. The physics interaction has been generated at the position (0, 0, 0), and the beam spot constraint has been turned on for the purpose of this study.

Figure 1.14(right) shows the resolution of the primary vertex position versus the number of tracks originating from the primary interaction. The resolution is better than X μm for low multiplicity events and approaches Y μm for high multiplicity events.

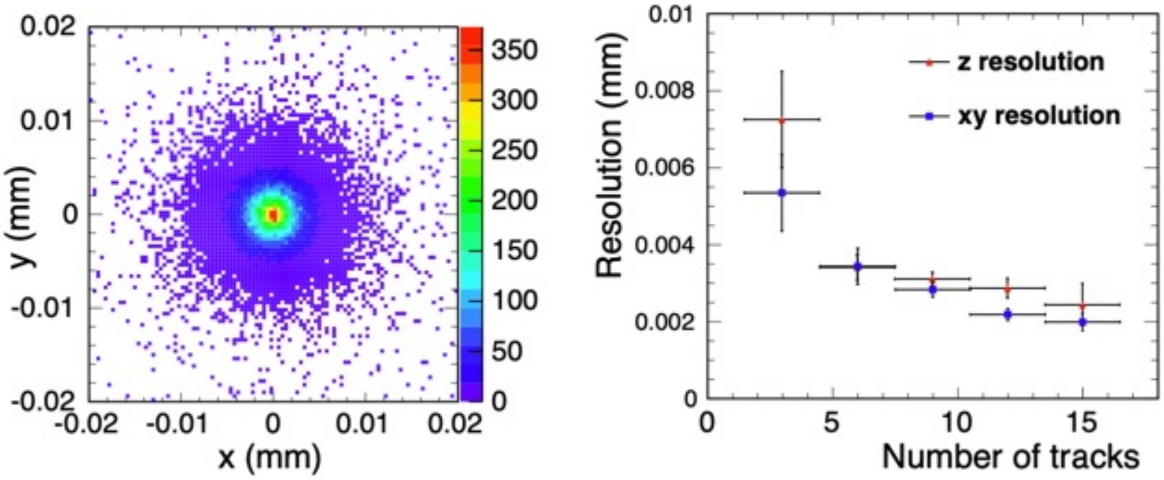

Figure 1.14: Position of the reconstructed primary vertex (left) and resolution of the primary vertex position as a function of the number of tracks originating from that vertex (right).

Figure 1.15 shows the transverse (a) and longitudinal (b) components of the secondary vertices as a function of the distance from the IP.

The overall vertexing performance for the Reference Detector is excellent, as expected already from the single track impact parameter resolutions.

1.2.5 Jet Flavor Tagging - traditional way (Chenguang Zhang, et al.)

Description of Jet Flavor Tagging framework/algorithm.

The ability to tag bottom, charm, and strange decays with high purity is a crucial aspect in the design of the vertex detector. Figure below shows the b-tagging efficiency of a light quark sample (red curve) or a charm quark sample (green curve) or a strange quark sample (yellow curve) versus the b-tagging efficiency of a bottom quark sample. The neural networks have been trained on a sample of di-jets at sqrt(s) = 91 GeV and tested on a statistically independent sample.

1.2.6 Jet Origin ID (Manqi Ruan, Kaili Zhang, et al.)

Description of Jet Origin ID framework/algorithm and performance.

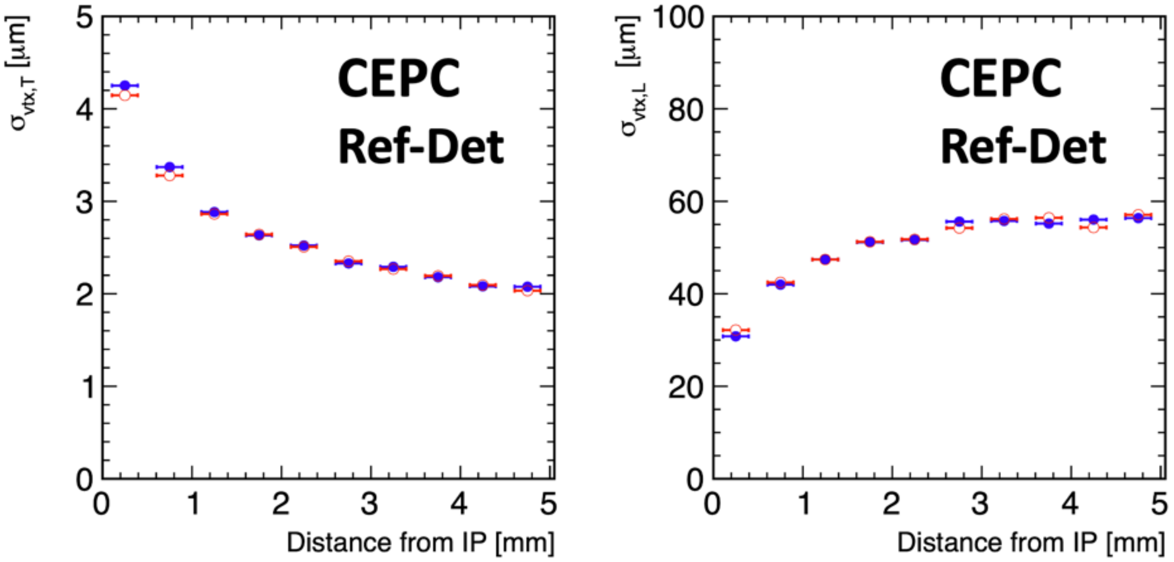

Figure 1.15: (Left) Resolution of the transverse component of secondary vertices as a function of the distance from the IP and the same for the longitudenal component in (Right)

1.3 Physics Benchmarks

Results of detailed simulation studies of the CEPC detector are discussed in this chapter. The generation of the events and common analysis tools used for the benchmark analyses are described briefly.

The production of events for the benchmarking analyses includes generation of a comprehensive set of Standard Model processes taking into account the CEPC beam spectrum, full Geant4 detector simulation, generation, simulation and mixing of machine-induced background processes with the signal samples and PFA-based reconstruction of the mixed events. Benchmark studies were conducted at a center-of-mass energy of 240 GeV using a dataset of 20 ab-1, at a center-of-mass energy of 91 GeV using a dataset of xx ab-1, and at center-of-mass energy of 350 GeV using a dataset of xx ab-1, separately. In these analyses, the SM Higgs mass was set to 125 GeV and the top quark mass was set to 17X GeV.

1.3.1 Event Generation **(Kaili Zhang, Gang Li, et al.)**

1.3.1.1 Monte Carlo event generators

The WHIZARD Monte Carlo event generator was used for the generation of all 2 $\rightarrow$ n processes, n = 2...6, where n is the number of final state fermions (e, μ, τ, u, d, s, c, b). The Higgs branching ratios listed in [ref] were assumed for the event generation.

1.3.1.2 Generated signal and background samples

1.3.2 Analysis Tools

To reconstruct jets in hadronic final states, the Durham algorithm as implemented from the FastJet [ref] package was used.

1.3.2.1 Multivariate analysis tools

The traditional approach in high energy physics to separate a signal from backgrounds is based on a set of fixed cuts. However, for complex final states and large backgrounds this method is often not optimal. Hence multivariate analysis techniques like artificial neutral networks or boosted decision trees (BDTs) are commonly used today. The implementations of these models in the TMVA [ref] software package were used for the benchmark analyses described in the following unless explicitly stated otherwise.

1.3.3 Higgs mass and production cross-section through recoil mass **(Mingshui Chen, et al.)**

1.3.4 Branching ratios of the Higgs boson in hadronics final states **(Yanping Huang, et al.)**

1.3.5 $H \to \gamma\gamma$ **(Yaquan Fang, et al.)**

1.3.6 $H \to invisible$ **(Mingshui Chen, et al.)**

1.3.7 Weak mixing angle **(Zhijun Liang, Bo Liu, et al.)**

1.3.8 A channel in flavor physics **(Shanzhen Chen, et al.)**

1.3.9 top mass and width **(Xiaohu Sun, et al.)**

1.3.10 W fusion cross section **(Hongbo Liao, et al.)**

1.3.11 Long-lived particles **(Liang Li, et al.)**

1.3.12 smuon **(Xuai Zhuang, et al.)**

1.3.13 $Z \to \mu\mu$

1.3.14 $H \to \mu\mu$

1.4 Challenges & Plan

1.4.1 Strategy for the measurement of absolute luminosity

It is necessary for absolute cross-sections and has relevant applications (e.g. n counting at the Z).

Is the measurement of absolute luminosity based only on Bhabha, how the luminometer is going to be used, is the measurement complemented by ee→gg events ?

Clearly outline the strategy for measuring absolute luminosity in the Ref-TDR

Precise knowledge of beam parameters is critical to the CEPC physics program. Luminosity and beam energy are measured by instrumentation close to the main detectors, which are described in more detail in Chapter 3 MDI.

Low-angle Bhabha scattering detected by dedicated calorimeters can provide the necessary precision for the integrated luminosity.

1.4.2 Plan of the use of resonant depolarization for W/Z mass

Beam energy measurements with an accuracy of (100-200) parts per million are needed for the determination of particle masses, including mtop, mW, and mZ. The plan on the use of resonant depolarization to measure the Z mass and W mass with high precision. These are key observables, whose precision must be improved in order to make full use of Higgs precision measurements (e.g. Higgs couplings)

A brief introduction to the operation scheme of polarized beams at $Z\&W$, for resonant depolarization measurements (refer to TDR for detailed description)

the $R\&D$ of a Compton polarimeter at BEPCII, and demonstration of resonant depolarization technique at BEPCII in the coming 2-3 years.

1.4.3 Methods & Considerations for Calibration, Alignment

1.4.4 Further technology decisions/detector optimization through physics performance studies

Brief mention how the physics performance studies influence further technology decisions/detector optimization.

1.5 Summary

A set of benchmarks have been conducted with the Ref detector with full simulation. They illustrate the detector performance for centre-of-mass energies in the range from 91 GeV up to 350 GeV. All results obtained have been summarized in following Table.